JACS
JOURNAL OF THE AMERICAN CHEMICAL SOCIETY
Article
pubs.acs.org/JACS

Fe/N/C Composite in Li–O_2 Battery: Studies of Catalytic Structure and Activity toward Oxygen Evolution Reaction

Jiang-Lan Shui,[†] Naba K. Karan,[‡] Mahalingam Balasubramanian,[‡] Shu-You Li,[§] and Di-Jia Liu*[,†]

[†]Chemical Sciences and Engineering Division and [‡]X-ray Science Division, Argonne National Laboratory, Lemont, Illinois 60439, United States

[§]Atomic and Nanoscale Characterization Experimental Center, Northwestern University, Evanston, Illinois 60208, United States

Supporting Information

ABSTRACT: Atomically dispersed Fe/N/C composite was synthesized and its role in controlling the oxygen evolution reaction during Li–O_2 battery charging was studied by use of a tetra(ethylene glycol) dimethyl ether-based electrolyte. Li–O_2 cells using Fe/N/C as the cathode catalyst showed lower overpotentials than α-MnO_2/carbon catalyst and carbon-only material. Gases evolved during the charge step contained only oxygen for Fe/N/C cathode catalyst, whereas CO_2 was also detected in the case of α-MnO_2/C or carbon-only material; this CO_2 was presumably generated from electrolyte decomposition. Our results reiterate the catalytic effect in reducing overpotentials, which not only enhances battery efficiency but also improves its lifespan by reducing or eliminating electrolyte decomposition. The structure of the Fe/N/C catalyst was characterized by transmission electron microscopy, scanning transmission electron microscopy, inductively coupled plasma optical emission spectroscopy, and X-ray absorption spectroscopy. Iron was found to be uniformly distributed within the carbon matrix, and on average, Fe was coordinated by 3.3 ± 0.6 and 2.2 ± 0.3 low Z elements (C/N/O) at bond distances of ~1.92 and ~2.09 Å, respectively.

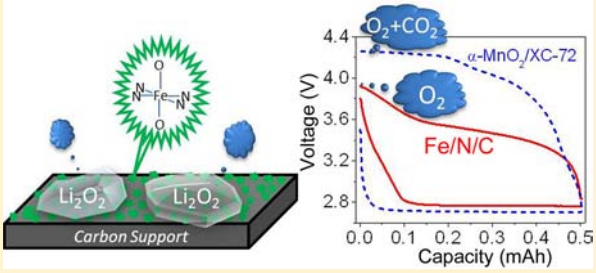

INTRODUCTION

The rechargeable Li–air battery represents an attractive energy storage device for electric vehicle applications due to its high theoretical energy storage capacity.[1−8] The use of an active cathode catalyst would reduce both discharging and charging overpotentials by facilitating the oxygen reduction reaction (ORR) during discharge and the oxygen evolution reaction (OER) during charge, thereby increasing the overall energy storage efficiency.[5,9−26] Although many studies have investigated the effects of cathode catalysts on the performance of Li–O_2 batteries, most of the early work used carbonate-based electrolytes (for example, propylene carbonate or PC), which have been recently proven to be unstable during cycling.[27−33] More recently, ether-based electrolytes [for example, tetra(ethylene glycol) dimethyl ether or TEGDME] have shown considerably improved stability during discharge–charge processes in Li–O_2 batteries. Li–O_2 battery reactions using such ether-based electrolytes were shown to involve Li_2O_2 during discharge and charge,[34−39] although the types of catalyst are yet to be fully explored. Furthermore, the role of the catalyst in promoting ORR (discharge) or OER (charge) in Li–O_2 batteries remains controversial.[39]

From a rational design point of view, an ideal cathode catalyst in the Li–O_2 battery should have highly active catalytic centers densely populated over the support surface, with minimum separation between individual sites, to achieve maximum interaction with the solid precipitate, such as Li_2O_2. The active sites should also be easily accessible to the electrons necessary to complete the electrochemical reactions. One such material is the transition metal–nitrogen–carbon composite prepared by thermolysis of transition metals (Fe, Co, etc.) ligated by nitrogen-containing organic compounds over high-surface-area carbon support.[40−44] For example, iron–nitrogen–carbon (Fe/N/C) catalysts have been synthesized and studied extensively as low-cost alternatives to Pt for ORR in both acidic and alkaline fuel cells.[45,46] Significant improvements in performance and durability have been reported recently for the Fe/N/C material, rendering it a benchmark for the nonprecious metal catalysts in fuel cell application.[41,47,48] Nonetheless, the nature of the active site and catalytic mechanism involved remain to be fully understood. One representative Fe/N/C catalyst is the material prepared by pyrolysis of supported iron(II) acetate and 1,10-phenanthroline that has demonstrated excellent activity toward ORR in the aqueous phase.[47,48] Since it is low-cost and easy to make, it is particularly attractive if such a catalyst can be used in promoting cathodic reactions in the Li–O_2 battery.

In this report, we demonstrate the improved performance of the rechargeable Li–O_2 battery when a Fe/N/C composite is used as the cathode catalyst. In side-by-side studies, we found that such a catalyst could reduce overpotentials during both

Received: June 19, 2012
Published: September 21, 2012

dx.doi.org/10.1021/ja3042993 | J. Am. Chem. Soc. 2012, 134, 16654−16661

discharge and charge processes when compared with the benchmark metal oxide catalyst, such as α-MnO_2 or high-surface-area carbon. Only oxygen was detected during the charging step when Fe/N/C was used as the cathode catalyst, whereas CO_2 was also found in comparable cells using α-MnO_2 or carbon under the same conditions. Li−O_2 batteries with Fe/N/C as the catalyst exhibited high cyclability (more than 50 cycles with excellent capacity retention). To ensure that only the Fe/N/C composite was present in promoting the catalytic reaction, we carried out thorough catalyst purification and an in-depth structural characterization using high-resolution imaging techniques and X-ray absorption spectroscopy. We found that Fe atoms were atomically and uniformly distributed over the carbon support, with the iron center ligated by nitrogen, oxygen, and possibly carbon in the graphite matrix.

EXPERIMENTAL SECTION

Catalyst Synthesis. Catalysts were synthesized following procedures reported in the literature, with minor modifications, using iron acetate ($FeAc_2$), 1,10-phenanthroline (phen), and high-surface-area carbon black [Black Pearls 2000, or BP with N_2 Brunauer−Emmett−Teller (BET) surface area 1467 m^2/g]. The $FeAc_2$ (95%) and phen were obtained from Aldrich, and they were both used without further purification. Typically, $FeAc_2$ and phen were first dissolved and mixed in ethanol at a molar ratio of 1:3 to form a Fe−phen complex. BP was also dispersed in ethanol, assisted by sonication, in a separate beaker. The two solutions were subsequently combined and stirred for 2 h at 60 °C, before drying overnight at 90 °C. The dried powder was ground in a planetary ball mill for 3 h at 400 rpm. This as-prepared catalyst precursor was labeled Fe/N/C-AP. A ceramic boat containing the milled Fe/N/C-AP powder was then placed in a tube furnace and heated at 1050 °C for 0.3 h under argon. The sample after the heat-treatment was labeled Fe/N/C-HT. It contained ∼1.3 wt.% iron. The heat-treated material was sonicated in 0.5 M H_2SO_4 to remove any metallic or metal oxide crystallites that might have formed during thermolysis. This was followed by a second heat-treatment at 700 °C for 0.5 h under N_2. The product thus obtained was labeled Fe/N/C-AT, which has also been referred to as the catalyst.

Caution: Thoroughly dried amorphous carbon powder as described above may catch fire with sudden exposure to ambient air. It is advisible to blank the powder with inert gas before removing the sample from the drying oven.

Li−O_2 Cell Assembly and Tests. The Li−O_2 cells used for this study had a Swagelok configuration similar to those reported in the literature.[11] For the cathode formulation, a slurry was prepared by mixing the catalyst and poly(vinylidene fluoride) (PVDF) binder at a weight ratio of 80/20. The slurry was painted uniformly onto a circular (12 mm diameter, 1.1 cm^2) piece of carbon paper (Spectracarb, 2050A) with a fine brush and then dried overnight at 90 °C in a vacuum oven. Comparative electrodes made with α-MnO_2/carbon (α-MnO_2; 40 wt %, carbon = XC-72) or BP carbon black were also prepared in a similar way. Loading of catalysts and carbons was between 0.5 and 2.0 mg on each cathode. Li foil was used as the anode and a circular porous glass fiber filter (Whatman, $^1/_2$ in. diameter) was used as the separator. The electrolyte was 1 M $LiCF_3SO_3$ (99.995% pure) in TEGDME (Aldrich). $LiCF_3SO_3$ was dried in a vacuum oven in a glovebox before use. Analytical-grade TEGDME was treated by distillation and molecular sieve before use. Both electrodes and the separator were stacked into a half-inch Swagelok union, which was placed inside a sealed glass cell. For cycling test, the glass cell was filled with oxygen accessible to the cathode layer through an open-end connector. The discharge/charge cycling was controlled by a Maccor system under a constant current of 0.05 mA with limited duration of 5 or 10 h for single discharge and charge. Cutoff voltage limits were 2.3 V for discharge and 4.4 V for charge. During cell preparation, particular attention was paid to the choice of carbon paper for the cathode: it was free of preloaded carbon particles to avoid any interference in the measured catalytic activity (see Supporting Information).

Characterizations. Imaging studies via transmission electron microscopy (TEM)/scanning transmission electron microscopy (STEM) with elemental analysis by energy-dispersive X-ray spectroscopy (EDX) were performed on an analytical scanning transmission atomic resolution electron microscope (JEOL JEM-2100F FAST TEM). For TEM and STEM measurements, powder samples were dispersed in ethanol by sonication before being applied onto copper grids. More than 10 points on each of several catalyst particles were examined to ensure that the results were statistically representative. Scanning electron microscopic images were taken on a Hitachi S4700-II microscope. Catalyst composition was analyzed via inductively coupled plasma optical emission spectroscopy (ICP-OES). The catalyst surface area was measured by the Brunauer−Emmett−Teller (BET) method at liquid nitrogen temperature with a Micromeritics ASAP2020 surface area and pore size analyzer.

X-ray absorption spectroscopy (XAS) measurements at the Fe K-edge were performed on Fe/N/C samples at sector 20BM of the Advanced Photon Source at Argonne National Laboratory. Both transmission and fluorescence data were collected by use of a gas ionization chamber detector or a Ge−multielement detector. The powders were capped in a cutout sample holder with Kapton tape on each side. Fe K-edge measurements were also performed on selected iron standards—Fe_3O_4 (Sigma−Aldrich), γ-Fe_2O_3 (Alfa Aesar), α-Fe_2O_3 (Sigma−Aldrich), iron(II) phthalocyanine (dye content ∼90%, Sigma−Aldrich), and iron(II) acetate, anhydrous (Fe 29.5% min, Alfa Aesar)—that were intimately mixed with carbon/boron nitride powder and made into pellets. Monochromatic X-rays were obtained by use of a fixed-exit Si (111) double crystal monochromator. The monochromator energy was calibrated with an Fe foil spectrum, and the inflection point (first-derivative maximum at the edge) was set at 7110.75 eV. A rhodium-coated X-ray mirror was used to suppress higher-order harmonics. The relative uncertainty in energy values during the XAS measurement was within ±0.05 eV. The standard procedure was used for X-ray absorption near-edge structure (XANES) and extended X-ray absorption fine structure (EXAFS) data reduction and processing. EXAFS structural parameters were obtained by nonlinear least-squares (NLS) analysis of the data using phase and amplitude functions generated from the FEFF6 code. The least-squares fits were performed in *r*-space by use of the analysis package IFEFFIT. A Gaussian distribution of bond distances was assumed for the EXAFS analysis.

For the analysis of gaseous products generated during the charging step, the test cells were first discharged for 10 or 5 h in O_2 atmosphere, and then the oxygen was completely flushed out by ultra-high-purity helium. A gas sample was taken from the cell at this point for the background analysis to make sure that oxygen was completely removed before the charging process was started. Gas effluents sampled for the background analysis and produced during the charging step (after 10 or 5 h charge in He atmosphere) were analyzed by gas chromatography (GC, HP 5890 Series II). The GC retention time was calibrated with the standard reference gases. See Supporting Information for more details on gas sampling and analysis.

RESULTS AND DISCUSSION

Structural Study of Fe/N/C Catalyst. For the present investigation, it was critically important to have a well-defined catalyst that is free from metallic or oxide particles that may have been formed during thermolysis. Although the Fe/N/C catalyst has been studied extensively in fuel cell applications, the nature of its active-site structure remains to be fully understood.[47,48] After pyrolysis at elevated temperature, the organic component in the organometallic precursor was fully decomposed and fractions of nitrogen and carbon were integrated into the carbonaceous support, together with atomically dispersed iron, to form the catalytically active centers embedded into the carbon support.[46] To understand

dx.doi.org/10.1021/ja3042993 | J. Am. Chem. Soc. 2012, 134, 16654−16661

this process, we carefully characterized the Fe/N/C samples at the different stages of preparation using TEM, STEM, EDX, ICP-OES, and XAS methods.

TEM examination of Fe/N/C-HT samples revealed little morphological difference from that of carbon support, and it detected no obvious metal crystallites (see Figure S1a in Supporting Information), presumably due to the low Fe loading and the short duration of the heat treatment. STEM study found, however, the existence of nanoparticles, as labeled by arrow 1 in Figure 1a. EDX detected a very strong iron signal

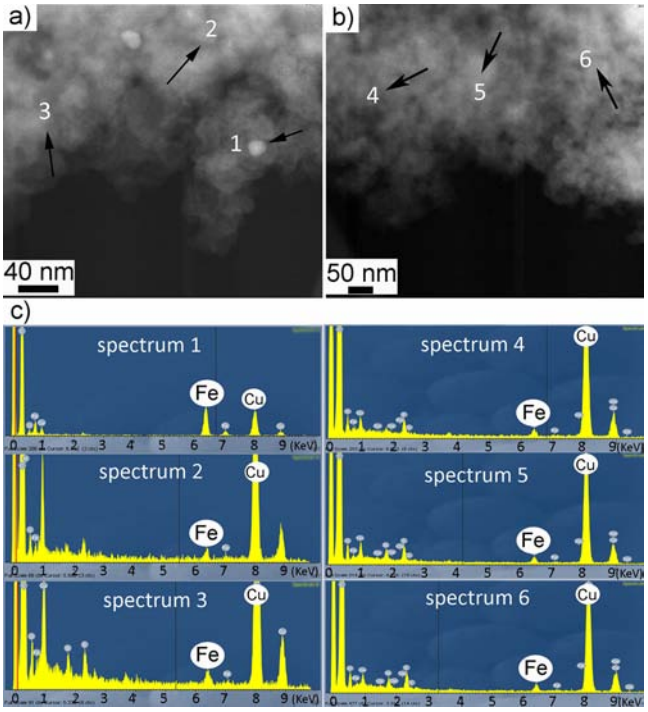

Figure 1. STEM images of (a) Fe/N/C-HT and (b) Fe/N/C-AT. The corresponding EDX spectra at positions 1–6 as indicated on STEM images are shown in panel c. Iron-rich particles disappeared after the acid wash.

from these particles, with reference to the copper signal from the sample grid, as is shown in spectrum 1 in Figure 1c. Additional high-resolution TEM study found that these iron-rich particles appeared to be amorphous and they lacked lattice structure (see Figure S1c, Supporting Information).

When the EDX beam is focused on areas where no such particles were present, such as positions 2 and 3 in Figure 1a, an Fe signal was still detected, albeit at a much weaker intensity, as shown by spectra 2 and 3 in Figure 1c. Figure 1b shows that all iron-rich particles in the Fe/N/C-HT sample disappeared after the acid wash. However, EDX detected the presence of iron throughout the sample, as indicated by random sampling marked by arrows 4, 5, and 6 in Figure 1b. The Fe signal strengths at these spots were similar to those in the non-particle region before the acid wash (spectra 2 and 3). Additional measurements were conducted at several places on the catalysts and the results were similar. ICP-OES analysis found that the weight percent of iron in Fe/N/C-HT and -AT was 1.3 and 0.39 wt %, respectively, suggesting that ~30% of iron survived the acid wash. A baseline ICP-OES analysis of untreated BP found a trace amount Fe, less than 0.01 wt %. The nitrogen adsorption isotherm measurement found that Fe/N/C-AT had a BET surface area of 562 $m^2 \cdot g^{-1}$. If a uniform site distribution over all micro- and mesopore surfaces accessible by the BET approach is assumed, we estimate that the surface site density of the Fe/N/C was approximately 7.5×10^{12} cm^{-2}, with ~7.3 nm separation between the neighboring centers. Actual site density could be significantly higher, since the molecular dimension of Fe–phen complex is considered too large to fit inside certain micropores by wet impregnation during catalyst synthesis.

We also used the XAS technique to study the electronic and atomic structures of Fe/N/C systems at various stages of preparation since the method is element-specific and sensitive to highly dilute constituents. Figure 2a shows the normalized

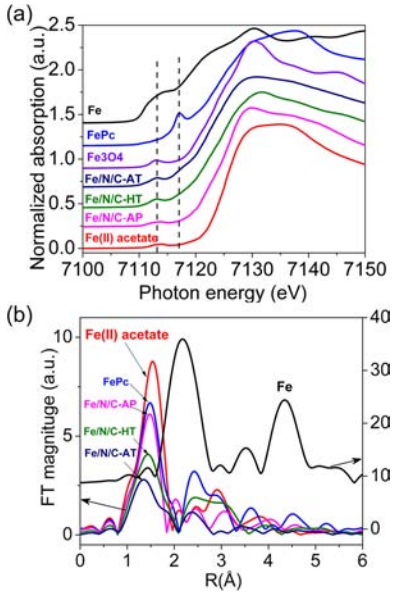

Figure 2. (a) Normalized XANES of Fe/N/C-AP, -HT, and -AT with reference compounds at the Fe K-edge. (b) Magnitudes of k^3-weighted Fourier-transformed (phase-uncorrected) EXAFS data for Fe/N/C-AP, -HT, and -AT with some reference compounds.

XANES at Fe K-edge of the Fe/N/C-AP, -HT, and -AT samples, together with several related reference compounds. The XANES spectra show that the Fe environment in Fe/N/C-AP is clearly different from $FeAc_2$, suggesting that the ligation changes from Fe–O to Fe–N during the formation of Fe–phen complex. In Fe/N/C-HT and -AT XANES spectra, the steeply rising feature before the main edge as seen for metallic iron and iron carbide is clearly missing, suggesting the absence of elemental Fe and/or iron carbide.[49]

The features in the XANES have been useful in obtaining information about the site symmetry around Fe in various macromolecular complexes.[50,51] In general, the presence of the strong feature at ~7118 eV is a fingerprint of Fe^{2+} square planar complexes, such as iron(II) phthalocyanine (FePc) and iron *meso*-tetrakis(phenyl)porphyrin.[52] Any deviation from perfect square planarity results in a substantial reduction of this feature. In addition, appearance of the pre-edge feature at ~7113 eV suggests the presence of axial ligand(s) (commonly bridging O and/or hydroxyl/water).[51] For the current set of samples, particularly for Fe/N/C-HT and -AT, the presence of prominent pre-edge feature at ~7113 eV suggests that the majority of the Fe centers in these samples were present in non-square planar configurations through an axial ligation, which is consistent with an average ligation number higher than

dx.doi.org/10.1021/ja3042993 | J. Am. Chem. Soc. 2012, 134, 16654–16661

4 derived from the EXAFS analysis (below). One caveat to the above observation is the presence of a small residual intensity at ~7118 eV for Fe/N/C-AT. As XAS is an averaging technique (i.e., site symmetry is averaged over all possible configurations), the presence of minor distorted square planar configurations could not be ruled out completely.

Figure 2b shows the Fourier-transformed magnitudes (phase-uncorrected) of k^3-weighted Fe K-edge EXAFS of Fe/N/C-AP, -HT, and -AT samples, together with those of the reference compounds. The coordination environment around Fe in Fe/N/C-AP is quite different from that in $FeAc_2$, suggesting again the ligand exchange from O to N in phen occurred during the synthesis. Appearance of substantially stronger peaks between 2.2 and 3.6 Å in Fe/N/C-HT in comparison to -AP and -AT samples, suggests the presence of some iron oxide after air exposure at the ambient temperature following the heat treatment. Details of the EXAFS analysis and the local structural parameters around Fe centers in these samples are given in Tables S2 and S3 in Supporting Information. Combining XANES linear summation and EXAFS analysis, we conclude that about 30 at. % of iron in Fe/N/C-HT sample is in the form of iron oxides containing predominantly Fe^{3+} species (see Figures S6 and S7 in Supporting Information). Evidently, the acid wash removed iron oxide(s) and a certain portion of ligated iron during the transformation of Fe/N/C-HT to Fe/N/C-AT. This observation is consistent with Figure 1, where Fe-rich particles were observed to be removed after the acid wash. After heat-treatment and acid wash, substantial reduction of the first peak intensity was observed, along with a concomitant asymmetric broadening of the peak, suggesting increased disorder and the potential presence of two distinctly different Fe−low Z element (C/N/O) bond distances in the first coordination shell. NLS analysis of EXAFS data for Fe/N/C-AT sample (see Supporting Information) also suggested two Fe−low Z element (C/N/O) bond distance contributions to the first coordination shell surrounding Fe: the first one with a shell radius (R) of ~1.92(2) Å and coordination number (CN) of 3.3 ± 0.6 and the second one with R = ~2.09(3) Å and CN = 2.2 ± 0.3. This coordination structure is consistent with the nonplanar site symmetry (averaged over all sites) results from XANES. Although EXAFS analysis could not unambiguously distinguish the contribution from C, N, or O, coordination of N or O to ionic Fe is most common. We therefore attribute the two shells to atomic nitrogen and oxygen. The local structure around Fe in the Fe/N/C-HT and -AT samples obtained from current analysis should also be compared to the previous EXAFS studies where Fe bonded to four nitrogens was found in a heat-treated sample with $FeSO_4$ and phenanthroline as precursors.[53,54] The present analysis showed that both Fe/N/C-HT and -AT samples have contributions from two immediate Fe−low Z element coordination shells, albeit from a different Fe source (iron acetate). Four-N-coordinated Fe has also been speculated to be the catalytic center in heat-treated (both in Ar and in NH_3) catalyst samples with iron(II) acetate and phenanthroline precursors, even though such an Fe environment has been recognized to be incomplete.[47] On the other hand, an octahedrally coordinated iron environment has been proposed for the heat-treated (in Ar) FeTMPPCl catalysts from Mossbauer measurements.[55]

For Li−O_2 battery performance evaluation, only Fe/N/C-AT was used as the cathode catalyst. For simplicity, Fe/N/C-AT is referred to as Fe/N/C catalyst for the remaining discussion.

Catalytic Performance Evaluation of Fe/N/C in Li−O_2 Batteries. The actual effect of catalyst in promoting cathodic reactions in Li−O_2 battery is somewhat contentious at present. Most of the studies on the cathode catalysis have been performed by using carbonate-based electrolytes, such as PC, until it was shown recently that such electrolytes are unstable under discharge−charge conditions. The observed activity was believed to be dominated by electrolyte decomposition (i.e., electrochemical reactions of the electrolyte in the presence of reduced O_2 species) instead of the formation/decomposition of Li_2O_2 and/or Li_2O.[27,28,31] Ether-based electrolytes (salts dissolved in dimethoxyethane; TEGDME) were claimed to be more stable than carbonate-based ones, although they are not completely immune to decomposition under deep discharge−charge conditions.[34,35,39,56] Several groups have found Li_2O_2 as the dominant product in discharge with ether-based electrolytes.[35−37] By limiting the discharging depth before switching to charging, McCloskey et al.[39] detected a considerable amount of O_2 produced via OER at the initial stage of charge and only a limited amount of CO_2 at charging voltage above 4.0 V over several benchmark catalysts. Investigation of the catalytic effect, therefore, should be under controlled discharge/charge depths to limit interference from side reactions.[57] At present, literature reports on such type of study are still scarce. Only limited studies on charge−discharge cycling facilitated by the catalyst using such electrolytes have started to appear.[58,59]

We applied Fe/N/C composite in the Li−O_2 battery cathode using an ether-based electrolyte and investigated its catalytic activity through comparison with some benchmark materials. TEGDME was used as the electrolyte solvent, and cells were discharged/charged under constant current of 0.05 mA. In a typical experiment, the cell was first "conditioned" by running two complete discharge−charge cycles (5-h duration for both discharge and charge) in oxygen, followed by another 10-h discharge (0.5 mA·h, corresponding to a capacity of 550 mA·h/g with 0.9 mg of Fe/N/C catalyst used). Subsequently, the oxygen in the cell was completely flushed out by high-purity helium until the gas sample taken from the cell showed no oxygen left. Afterward, the cell was subject to 10-h charging under constant current, and the gas sample was taken from the cell for GC analysis at the end.

The first catalyst used for the comparison study was α-MnO_2/XC-72. Since it was first reported by Débart et al. in 2008,[14] carbon-supported α-MnO_2 has become a benchmark catalyst for Li−O_2 batteries. Figure 3a shows representative discharge−charge load curves of two Li−O_2 cells containing Fe/N/C and α-MnO_2/XC-72 cathode catalysts, respectively. During the discharge, the cell containing Fe/N/C catalyst demonstrated a slight reduction in overpotential over that with α-MnO_2/XC-72, indicating improvement in the catalytic activity of promoting lithium peroxide formation through ORR. In the following charge step, however, the effect of the catalyst became more apparent. The cell with Fe/N/C composite showed lower potential through nearly the entire charging span compared to that with α-MnO_2/XC-72 catalyst, and a reduction in the overpotential of as much as 0.6 V was seen at the middle of charge step.

The cells were cycled over a controlled capacity of 0.5 mA·h. Periodically, GC analyses were performed to measure the composition of the gas released at the end of selected charging cycles following the procedure described in the Experimental Section. Figure 3b shows a side-by-side comparison of the GC

dx.doi.org/10.1021/ja3042993 | J. Am. Chem. Soc. 2012, 134, 16654−16661

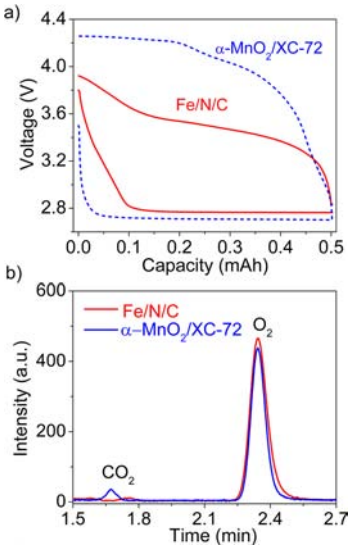

Figure 3. (a) Discharge/charge voltage profiles of Li−O_2 cells using α-MnO_2/XC-72 and Fe/N/C as cathode catalysts. (b) Representative GC signals as a function of retention time for the gas effluents collected at the end of the charging processes of panel a.

analyses at the end of the third charging cycle. Only oxygen was released from the cell with Fe/N/C catalyst, whereas both O_2 and CO_2 were found in the gas from the cell with α-MnO_2/XC-72 as the catalyst. The GC analysis results for oxygen are also listed in Table 1, together with the theoretical production of O_2

Table 1. O_2 Evolved during Charging Process in He after Cells Were Predischarged in O_2

gas samples		quantity of O_2 (mL)	
electrochemical capacity (mA·h)	cathode	measured	theoretical
0.5	Fe/N/C	0.210[a]	0.224
0.5	α-MnO_2/XC72	0.200[a]	0.224
0.25	Fe/N/C	0.100[b], 0.104[c], 0.059[d]	0.112
0.25	BP	0.093[b]	0.112

[a]Average of the first three cycles. [b]At the end of the third cycle. [c]At the end of the 20th cycle. [d]At the end of 50th cycle, 0.013 mL of CO_2 was also detected in the gas sample.

based on decomposition of Li_2O_2 during charging (see Supporting Information). The oxygen released by the average of the first three charging cycles is in good agreement with the theoretical value, indicating a near-complete reversibility of the cell using Fe/N/C as catalyst. In fact, the cell continued to demonstrate good reversibility as the cycling progressed. However, when the battery approached the end of its cycle life, we did observe the production of CO_2 in the effluent gas during charging, an indication of electrolyte decomposition. More details are discussed in the section below.

The differences in charging potential and gas effluent between the two systems are striking, particularly in reference to the recent investigations on several catalyst systems including α-MnO_2, Au, and carbon black.[35,39] In these studies, production of a small amount of CO_2 was detected at high charging voltage (>4 V) for a variety of catalysts, which is consistent with our observation on α-MnO_2/XC-72. Why, then, was the formation of CO_2 avoided when Fe/N/C composite was used as the catalyst?

In an ideal Li−O_2 battery, the following reaction should be completely reversible at the cathode surface:

$$2Li^+ + 2e^- + O_2 \leftrightarrow Li_2O_2 \quad (1)$$

In the case of α-MnO_2/C catalyst, the previous study suggested that CO_2 production was contributed through electrolyte decomposition where the potential was above 4 V.[35] We believe that reduction of overpotential by Fe/N/C catalyst during OER is the primary reason for CO_2-free effluent in the charging step.

Fe/N/C is a known ORR catalyst, with activity close to that of Pt in aqueous acidic electrolyte[47] and better than that of MnO_x/C in alkaline media.[45,46] Its improved OER activity over α-MnO_2/XC-72 in Li−O_2 battery may come from structural advantages. In α-MnO_2/XC-72, the manganese oxide particles were typically agglomerated together with single particle size of 100 × 200 nm, as shown in Figure 4. The oxide particles are

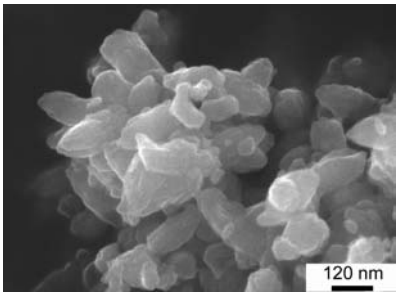

Figure 4. SEM image of an agglomerate of α-MnO_2 nanoparticles in α-MnO_2/XC-72 catalyst.

physically mixed with carbon nanoparticles with limited interfacial contact. α-MnO_2 itself is not an efficient electronic conductor. One would therefore expect that the solid lithium peroxide precipitates, should they be formed either on the surface of submicrometer α-MnO_2 or on the carbon, would encounter a high barrier for electrocatalytic decomposition due to inefficient electron or mass transfers. Such a barrier would lead to high polarization and, hence, high overpotentials. In contrast, Fe/N/C has atomically dispersed, molecular-dimension active sites embedded throughout the conductive substrate with high surface density. Such a catalyst could produce a higher interfacial boundary with the lithium oxide precipitates, thereby lowering both electron and mass transport barriers and reducing the overpotentials during charging.

The second catalyst used for the comparison study was uncatalyzed carbon, BP. A recent study found that pure carbon (XC-72) had similar charging profile and lower CO_2 production compared with supported nanoparticle catalysts (Au and MnO_2) in nonaqueous Li−O_2 batteries using dimethoxyethane (DME) as the electrolyte.[39] Since there exist a variety of carbons with different morphologies that may affect catalytic activity, it was most appropriate for us to compare with the same carbon used for preparing the Fe/N/C catalyst. We found, indeed, that BP alone could produce a fairly low overpotential, in particular at the onset of the charging step. A side-by-side comparison with Fe/N/C, however, showed overall improvement in both ORR and OER after iron and nitrogen doping. Figure 5 shows the reduction in both charge and discharge overpotentials of Fe/N/C over BP in a multicycle test. The cells were cycled under controlled capacity

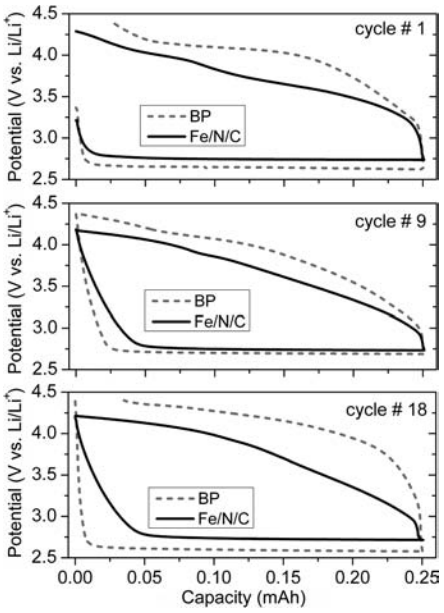

Figure 5. Load profiles of cells at first, ninth, and 18th discharge–charge cycles. Fe/N/C and BP were used as cathode materials. Current was 0.05 mA with duration of 5 h, corresponding to capacity of ~500 mA·h/g.

at 0.25 mA·h (500 mA·h/g for 0.5 mg of catalyst). After initial conditioning through cycle 1, the overpotentials reduced gradually to the lowest levels for both Fe/N/C- and BP-based cells at cycle 9 (Figure 5b) before steadily increasing with continued cycling. This change was especially drastic for the cell with BP in the cathode (from ninth to 18th cycle). This cell failed soon thereafter, with a significant fraction of the charging span occurring at above 4 V. In contrast, the voltage profiles of the cell with Fe/N/C catalyst changed only slightly during the same course.

GC measurements were also used to compare the gas compositions formed in the charge step from the cell with Fe/N/C and its carbon-only counterpart. Representative GC plots taken at the end of the third charging cycle for both materials are shown in Figure 6. The cells and the gas samples were

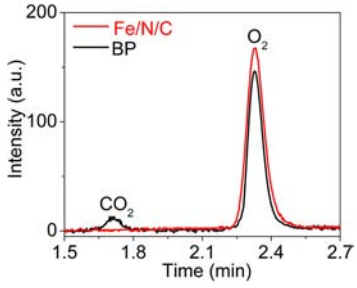

Figure 6. Representative GC measurements of BP and Fe/N/C for the gas effluents collected at the end of the third charging cycle.

prepared in a similar way as those outlined for Figure 3b, except that 5-h (0.25 mA·h) instead of 10-h (0.5 mA·h) discharge–charge and a lower amount of catalyst were used. We observed predominantly O_2 production, with a small amount of CO_2 for the BP cathode. No CO_2 was detected for the Fe/N/C-based cell. The amount of evolved O_2 was in good agreement with the theoretical value; (see Table 1). The difference in gas composition could once more be ascribed to the difference in the cell overpotentials.

A side-by-side comparison on the cycle lifespan was also carried out for Fe/N/C- and BP-based Li–O_2 battery cells. Discharge–charge depths were controlled by limiting the durations of both processes to 5 h. Their capacities, as a function of discharge–charge cycle number, are plotted in Figure 7. The cell with Fe/N/C as catalyst continued to nearly

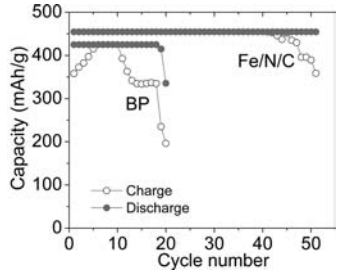

Figure 7. Cycling performance of cells with catalysts Fe/N/C and carbon black (BP) as cathode catalysts. Current was 0.05 mA with duration of 5 h.

50 cycles with a stable capacity, whereas the cell with BP failed before the 20th cycle. The cycling measurements in Figure 5, combined with the load curves at the selected cycle number, suggested a strong correlation between the reduced overpotentials and extended battery lifespan. Decorating the carbon surface with atomic Fe and N had clearly facilitated the OER and, to a lesser degree, ORR processes by reducing the overpotentials at the Li–O_2 battery cathode. The Fe/N/C catalyst had, thereby, alleviated the detrimental effects associated with electrolyte decomposition and prolonged the battery life.

We also performed GC analysis of the gas effluents from the cell with Fe/N/C catalyst at the end of the 20th and 50th cycles. At the end of the 20th cycle, oxygen evolution was still very close to the theoretical value and no CO_2 was detected. At the 50th cycle, CO_2 was detected, although O_2 still represented the dominant component in the charging gas (Figure S10, Supporting Information). These results are also given in Table 1. This observation indicated that electrolyte decomposition occurred near the end of the cycling test, although OER of Li_2O_2 remained as the main process during the charging step, which was also confirmed by an XRD study (Figure S11, Supporting Information). Appearance of CO_2 near the end of the battery lifespan was not surprising. Even though Fe/N/C catalyst had reduced the overpotentials and, thus, the side reactions under both charging and discharging conditions, one could not preclude trace amounts of byproducts formed through TEGDME–O_2 reaction.[35,56] Such byproducts are insoluble in the electrolyte and not entirely electrocatalytically decomposable. They accumulated slowly over the cathode, insulating the catalytic sites and leading to a gradual increase in overpotentials during cycling. As the portion of the charging profile at >4 V steadily increases, more electrolyte decomposition can be expected as the side reaction to OER of Li_2O_2.[39] Similarly, low-level CO_2 production was also observed in the battery with Fe/N/C catalyst when it was subjected to "deep" discharge–charge conditions (discharging to 2.2 V followed by charging to 4.5 V, with a capacity of ~4300 mA·h/g).[35,56] The Fe/N/C catalyst, though still more efficient in lowering the charging potential than MnO_2 and BP (Figure

dx.doi.org/10.1021/ja3042993 | J. Am. Chem. Soc. 2012, 134, 16654–16661

S12, Supporting Information), also produced CO_2 by decomposing TEGDME under this condition. (Figure S13, Supporting Information) An analysis of relevant catalytic processes is also given in Supporting Information.

CONCLUSIONS

An iron−nitrogen−carbon composite was synthesized and its catalytic performance was evaluated for the first time in connection with rechargeable Li−O_2 battery application. Extensive structural characterization, by high-resolution imaging and X-ray absorption spectroscopic techniques, identified high-density, atomically dispersed active sites embedded in the carbon matrix in the purified catalyst. This chemically modified carbon produced lower charge−discharge overpotentials and significantly improved the battery lifespan when compared with the well-studied α-MnO_2/XC-72 and its unmodified carbon-only counterpart. Effluent gas analysis at the end of controlled discharge−charge cycles found no CO_2 formation for cathode made of Fe/N/C catalyst, suggesting it selectively promoted the decomposition of lithium peroxide over that of the electrolyte. Such improved selectivity led to an enhanced battery lifespan under controlled cycling, with 50 discharge−charge cycles achieved. Reversible Li_2O_2 formation and decomposition remained the dominant processes at the end of battery cycling life, although some electrolyte decomposition was observed. This study reiterates the importance and promise of developing efficient electrocatalysts for Li−O_2 battery application, particularly those that can promote the oxygen evolution reaction through better mass and electronic transfers.

ASSOCIATED CONTENT

Supporting Information

Additional text, 13 figures, and two tables providing structure elucidation of the catalysts through TEM imaging and XAS analyses, measurement of gas effluent of charged batteries, and other experimental details. This material is available free of charge via the Internet at http://pubs.acs.org.

AUTHOR INFORMATION

Corresponding Author

djliu@anl.gov

Notes

The authors declare no competing financial interest.

ACKNOWLEDGMENTS

We thank Dr. Lynn Trahey for supplying α-MnO_2 catalyst and Drs. Peng Du and Zhengcheng Zhang for supplying the electrolyte used in this study. Financial support by the Grand Challenge program of Argonne National Laboratory is gratefully acknowledged. This work and the use of the Advanced Photon Source and the Electron Microscopy Center are supported by the Office of Science, U.S. Department of Energy, under Contract DE-AC02-06CH11357. The PNC/XSD facilities at the Advanced Photon Source are supported by the U.S. Department of Energy, Basic Energy Sciences, a Major Resources Support grant from NSERC, University of Washington, Simon Fraser University, and the Advanced Photon Source.

REFERENCES

(1) Abraham, K. M.; Jiang, Z. *J. Electrochem. Soc.* **1996**, *143*, 1.
(2) Bruce, P. G.; Freunberger, S. A.; Hardwick, L. J.; Tarascon, J. M. *Nat. Mater.* **2012**, *11*, 19.
(3) Bruce, P. G.; Hardwick, L. J.; Abraham, K. M. *MRS Bull.* **2011**, *36*, 506.
(4) Girishkumar, G.; McCloskey, B.; Luntz, A. C.; Swanson, S.; Wilcke, W. *J. Phys. Chem. Lett.* **2010**, *1*, 2193.
(5) Ogasawara, T.; Débart, A.; Holzapfel, M.; Novák, P.; Bruce, P. G. *J. Am. Chem. Soc.* **2006**, *128*, 1390.
(6) Read, J. *J. Electrochem. Soc.* **2002**, *149*, A1190.
(7) Zheng, J. P.; Liang, R. Y.; Hendrickson, M.; Plichta, E. J. *J. Electrochem. Soc.* **2008**, *155*, A432.
(8) Kraytsberg, A.; Ein-Eli, Y. *J. Power Sources* **2011**, *196*, 886.
(9) Lu, Y. C.; Xu, Z. C.; Gasteiger, H. A.; Chen, S.; Hamad-Schifferli, K.; Shao-Horn, Y. *J. Am. Chem. Soc.* **2010**, *132*, 12170.
(10) Débart, A.; Bao, J.; Armstrong, G.; Bruce, P. G. *J. Power Sources* **2007**, *174*, 1177.
(11) Cheng, H.; Scott, K. *J. Power Sources* **2010**, *195*, 1370.
(12) Lu, Y. C.; Gasteiger, H. A.; Parent, M. C.; Chiloyan, V.; Shao-Horn, Y. *Electrochem. Solid-State Lett.* **2010**, *13*, A69.
(13) Thapa, A. K.; Saimen, K.; Ishihara, T. *Electrochem. Solid-State Lett.* **2010**, *13*, A165.
(14) Débart, A.; Paterson, A. J.; Bao, J.; Bruce, P. G. *Angew. Chem., Int. Ed.* **2008**, *47*, 4521.
(15) Lu, Y. C.; Gasteiger, H. A.; Crumlin, E.; McGuire, R.; Shao-Horn, Y. *J. Electrochem. Soc.* **2010**, *157*, A1016.
(16) Trahey, L.; Johnson, C. S.; Vaughey, J. T.; Kang, S.-H.; Hardwick, L. J.; Freunberger, S. A.; Bruce, P. G.; Thackeray, M. M. *Electrochem. Solid-State Lett.* **2011**, *14*, A64.
(17) Kichambare, P.; Kumar, J.; Rodrigues, S.; Kumar, B. *J. Power Sources* **2011**, *196*, 3310.
(18) Ren, X. M.; Zhang, S. S.; Tran, D. T.; Read, J. *J. Mater. Chem.* **2011**, *21*, 10118.
(19) Zhang, S. S.; Ren, X. M.; Read, J. *Electrochim. Acta* **2011**, *56*, 4544.
(20) Lu, Y. C.; Kwabi, D. G.; Yao, K. P. C.; Harding, J. R.; Zhou, J. G.; Zuin, L.; Shao-Horn, Y. *Energy Environ. Sci* **2011**, *4*, 2999.
(21) Thapa, A. K.; Ishihara, T. *J. Power Sources* **2011**, *196*, 7016.
(22) Zhang, G. Q.; Zheng, J. P.; Liang, R.; Zhang, C.; Wang, B.; Hendrickson, M.; Plichta, E. J. *J. Electrochem. Soc.* **2010**, *157*, A953.
(23) Dong, S.; Chen, X.; Zhang, K. J.; Gu, L.; Zhang, L. X.; Zhou, X. H.; Li, L. F.; Liu, Z. H.; Han, P. X.; Xu, H. X.; Yao, J. H.; Zhang, C. J.; Zhang, X. Y.; Shang, C. Q.; Cui, G. L.; Chen, L. Q. *Chem. Commun.* **2011**, *47*, 11291.
(24) Cui, Y. M.; Wen, Z. Y.; Liu, Y. *Energy Environ. Sci.* **2011**, *4*, 4727.
(25) Lu, Y. C.; Gasteiger, H. A.; Shao-Horn, Y. *J. Am. Chem. Soc.* **2011**, *133*, 19048.
(26) Thapa, A. K.; Hidaka, Y.; Hagiwara, H.; Ida, S.; Ishihara, T. *J. Electrochem. Soc.* **2011**, *158*, A1483.
(27) Mizuno, F.; Nakanishi, S.; Kotani, Y.; Yokoishi, S.; Iba, H. *Electrochemistry* **2010**, *78*, 403.
(28) Freunberger, S. A.; Chen, Y. H.; Peng, Z. Q.; Griffin, J. M.; Hardwick, L. J.; Bardé, F.; Novák, P.; Bruce, P. G. *J. Am. Chem. Soc.* **2011**, *133*, 8040.
(29) Bryantsev, V. S.; Blanco, M. *J. Phys. Chem. Lett.* **2011**, *2*, 379.
(30) Xu, W.; Viswanathan, V. V.; Wang, D. Y.; Towne, S. A.; Xiao, J.; Nie, Z. M.; Hu, D. H.; Zhang, J. G. *J. Power Sources* **2011**, *196*, 3894.
(31) Xiao, J.; Hu, J. Z.; Wang, D. Y.; Hu, D. H.; Xu, W.; Graff, G. L.; Nie, Z. M.; Liu, J.; Zhang, J. G. *J. Power Sources* **2011**, *196*, 5674.
(32) Xu, W.; Xu, K.; Viswanathan, V. V.; Towne, S. A.; Hardy, J. S.; Xiao, J.; Nie, Z. M.; Hu, D. H.; Wang, D. Y.; Zhang, J. G. *J. Power Sources* **2011**, *196*, 9631.
(33) Cheng, H.; Scott, K. *Appl. Catal., B* **2011**, *108*, 140.
(34) McCloskey, B. D.; Bethune, D. S.; Shelby, R. M.; Girishkumar, G.; Luntz, A. C. *J. Phys. Chem. Lett.* **2011**, *2*, 1161.
(35) Freunberger, S. A.; Chen, Y. H.; Drewett, N. E.; Hardwick, L. J.; Bardé, F.; Bruce, P. G. *Angew. Chem., Int. Ed.* **2011**, *50*, 8609.
(36) Mitchell, R. R.; Gallant, B. M.; Thompson, C. V.; Shao-Horn, Y. *Energy Environ. Sci.* **2011**, *4*, 2952.

(37) Laoire, C. Ó.; Mukerjee, S.; Plichta, E. J.; Hendrickson, M. A.; Abraham, K. M. *J. Electrochem. Soc.* **2011**, *158*, A302.
(38) Read, J. *J. Electrochem. Soc.* **2006**, *153*, A96.
(39) McCloskey, B. D.; Scheffler, R.; Speidel, A.; Bethune, D. S.; Shelby, R. M.; Luntz, A. C. *J. Am. Chem. Soc.* **2011**, *133*, 18038.
(40) Wu, L. B.; Nabae, Y.; Moriya, S.; Matsubayashi, K.; Islam, N. M.; Kuroki, S.; Kakimoto, M.; Ozaki, J.; Miyata, S. *Chem. Commun.* **2010**, *46*, 6377.
(41) Wu, G.; More, K. L.; Johnston, C. M.; Zelenay, P. *Science* **2011**, *332*, 443.
(42) Jasinski, R. *Nature* **1964**, *201*, 1212.
(43) Yang, J. B.; Liu, D. J.; Kariuki, N. N.; Chen, L. X. *Chem. Commun.* **2008**, *3*, 329.
(44) Ma, S. Q.; Goenaga, G. A.; Call, A. V.; Liu, D. J. *Chem.—Eur. J.* **2011**, *17*, 2063.
(45) Meng, H.; Jaouen, F.; Proietti, E.; Lefèvre, M.; Dodelet, J. P. *Electrochem. Commun.* **2009**, *11*, 1986.
(46) Lima, F. H. B.; Calegaro, M. L.; Ticianelli, E. A. *J. Electroanal. Chem.* **2006**, *590*, 152.
(47) Lefèvre, M.; Proietti, E.; Jaouen, F.; Dodelet, J. P. *Science* **2009**, *324*, 71.
(48) Proietti, E.; Jaouen, F.; Lefèvre, M.; Larouche, N.; Tian, J.; Herranz, J.; Dodelet, J. P. *Nat. Commun.* **2011**, *2*, 416.
(49) Kopelev, N. S.; Chechersky, V.; Nath, A.; Wang, Z. L.; Kuzmann, E.; Zhang, B. S.; Via, G. H. *Chem. Mater.* **1995**, *7*, 1419.
(50) Stefan, I. C.; Mo, Y. B.; Ha, S. Y.; Kim, S.; Scherson, D. A. *Inorg. Chem.* **2003**, *42*, 4316.
(51) Kim, S.; Bae, I. T.; Sandifer, M.; Ross, P. N.; Carr, R.; Woicik, J.; Antonio, M. R.; Scherson, D. A. *J. Am. Chem. Soc.* **1991**, *113*, 9063.
(52) Pennerhahn, J. E.; Mcmurry, T. J.; Renner, M.; Latosgrazynsky, L.; Eble, K. S.; Davis, I. M.; Balch, A. L.; Groves, J. T.; Dawson, J. H.; Hodgson, K. O. *J. Biol. Chem.* **1983**, *258*, 2761.
(53) Bron, M.; Radnik, J.; Fieber-Erdmann, M.; Bogdanoff, P.; Fiechter, S. *J. Electroanal. Chem.* **2002**, *535*, 113.
(54) Charreteur, F.; Jaouen, F.; Ruggeri, S.; Dodelet, J. P. *Electrochim. Acta* **2008**, *53*, 2925.
(55) Schulenburg, H.; Stankov, S.; Schünemann, V.; Radnik, J.; Dorbandt, I.; Fiechter, S.; Bogdanoff, P.; Tributsch, H. *J. Phys. Chem. B* **2003**, *107*, 9034.
(56) Wang, H.; Xie, K. *Electrochim. Acta* **2012**, *64*, 29.
(57) Jung, H. G.; Hassoun, J.; Park, J. B.; Sun, Y. K.; Scrosati, B. *Nat. Chem.* **2012**, *4*, 579.
(58) Li, Y. L.; Wang, J. J.; Li, X. F.; Geng, D. S.; Banis, M. N.; Li, R. Y.; Sun, X. L. *Electrochem. Commun.* **2012**, *18*, 12.
(59) Trahey, L.; Karan, N. K.; Chan, M. K. Y.; Lu, J.; Ren, Y.; Greeley, J.; Balasubramanian, M.; Burrell, A. K.; Curtiss, L. A.; Thackeray, M. M. *Adv. Energy Mater.* **2012**, DOI: 10.1002/aenm.201200037.